

This item is the archived peer-reviewed author-version of:

Single particle deformation and analysis of silica-coated gold nanorods before and after femtosecond laser pulse excitation

Reference:

Albrecht Wiebke, Deng Tian-Song, Goris Bart, van Huis Marijn A., Bals Sara, van Blaaderen Alfons.- Single particle deformation and analysis of silica-coated gold nanorods before and after femtosecond laser pulse excitation

Nano letters / American Chemical Society - ISSN 1530-6984 - 16:3(2016), p. 1818-1825

Full text (Publishers DOI): <http://dx.doi.org/doi:10.1021/ACS.NANOLETT.5B04851>

To cite this reference: <http://hdl.handle.net/10067/1319240151162165141>

Single particle deformation and analysis of silica coated gold nanorods before and after femtosecond laser pulse excitation

Wiebke Albrecht,^{*,†} Tian-Song Deng,[†] Bart Goris,[‡] Marijn A. van Huis,[†] Sara Bals,[‡] and Alfons van Blaaderen^{*,†}

[†]*Soft Condensed Matter, Debye Institute for Nanomaterials Science, Utrecht University, Princetonplein 5, 3584 CC Utrecht, The Netherlands*

[‡]*Electron Microscopy for Materials Research (EMAT), University of Antwerp, Groenenborgerlaan 171, 2020 Antwerp, Belgium*

E-mail: W.Albrecht@uu.nl; A.vanBlaaderen@uu.nl

Abstract

We performed single particle deformation experiments on silica-coated gold nanorods under femtosecond illumination. Changes in the particle shape were analyzed by electron microscopy and associated changes in the plasmon resonance by electron energy loss spectroscopy. Silica-coated rods were found to be more stable compared to uncoated rods but could still be deformed via an intermediate bullet-like shape for silica shell thicknesses of 14 nm. Changes in the size ratio of the rods after fs-illumination resulted in blue-shifting of the longitudinal plasmon resonances. Two-dimensional spatial mapping of the plasmon resonances revealed that the flat side of the bullet-like particles showed a less pronounced longitudinal plasmonic electric field enhancement. These findings were confirmed by finite-difference time-domain (FDTD) simulations.

Furthermore, at higher laser fluences size reduction of the particles was found, also for particles that were not completely deformed yet.

Keywords

Gold nanorods, femtosecond laser excitation, deformation, EELS

Introduction

Gold nanorods (NRs) have attracted much scientific attention due to their unique optical and photothermal properties¹⁻⁵. These result in a wide range of applications in various fields, such as photoacoustic imaging^{6,7}, catalysis⁸, drug delivery⁹, (bio)sensing¹⁰⁻¹³, optical recording and data storage¹⁴⁻¹⁷ and hyperthermic cancer treatment therapy in medicine^{18,19}. Several of these applications can even be combined using the same particles, like imaging and photothermal therapy²⁰ or image-guided drug delivery and hyperthermia²¹, which makes gold nanorods even more versatile.

Localized surface plasmon resonances (LSPR) which are accompanied by efficient interactions of light with these nanoparticles which include strong local field enhancement of the particle tips lie at the core of many of those applications. Gold nanorods exhibit two distinct plasmon resonances, a transverse and a longitudinal one, because of their anisotropic shape and reduced symmetry compared to gold nanospheres. The transverse resonance, having a wavelength of approximately 520 nm, is the same as for spherical gold nanoparticles, whereas the longitudinal surface plasmon resonance depends strongly on the length to diameter aspect ratio of the nanorods. Therefore, it can be tuned to span the visible and near-infrared parts of the spectrum by changing the aspect ratio of the nanorods²²⁻²⁴.

When exciting the longitudinal plasmon resonance with an high energy and short nanosecond (ns) or femtosecond (fs) laser pulse the photon energy is absorbed by the electrons with subsequent electron-phonon scattering resulting in the heating of the particle. This electron-

phonon scattering takes on the order of 1-4 picosecond (ps) for gold nanoparticles²⁵. The heat is then released to the surrounding medium by diffusion, a process for which the time-scale strongly depends on the properties and geometry of the surrounding medium²⁶. It is well established that gold nanorods undergo an aspect ratio reduction, up to a complete deformation into a crystalline nanosphere or even fragmentation, after absorption of sufficient photons²⁷⁻²⁹. Furthermore, gold NRs can be deformed by thermal heating^{30,31}. The rate of heating and cooling and the final temperature of the particles are of crucial importance to the deformation mechanism and path followed. Petrova and coworkers inferred from their measurements that NRs that were deformed by fs-laser excitation did not show structural changes below 700 °C although the same particles already completely deformed at 250 °C when heated in an oven³². These findings were attributed to the rods not staying hot for long enough during pulsed laser irradiation. Indicating, as mentioned, that thermal diffusion plays an important role.

Most work so far aimed at understanding the light and heat induced deformation of Au nanorods was performed on large ensembles of these nanoparticles. Link et al. studied the dependence of the deformation on the laser pulse width and found that significantly less pulse energy is needed to deform and melt the particles when using fs-pulses compared to ns-pulses^{28,29}. This was explained by competitive cooling during the pulse duration of a ns-pulse. At high laser fluences fragmentation was observed. In related work the same group measured a threshold energy of about 60 fJ to melt single nanorods with an average length and width of 44 nm and 11 nm, respectively, by fs laser pulses in aqueous solution³³.

Zijlstra et al. showed that much information can be gained by performing single-particle measurements and thereby removing much of the heterogeneities of the sample³⁴. They used white light scattering spectroscopy and scanning electron microscopy to study the laser-induced melting of single gold nanorods. They measured a melting energy of 260 fJ for nanorods with an average size of 92×30 nm and inferred from their measurements that nanorods with larger aspect ratio are thermodynamically less stable as they were found to

deform more easily. Taylor et al. studied the reshaping behavior of individual nanorods under fs-laser illumination by scanning electron microscopy³⁵. They concluded that the reshaping process is driven by curvature-induced surface diffusion of Au atoms over the nanorod surface and that the stability of the rods decreases with increasing aspect ratio.

From these results it has become clear that correlating single-particle reshaping experiments with high-resolution electron microscopy and spectroscopy can reveal new insights into the atomistic mechanisms behind light induced particle deformations. In our paper we show additionally that if both single particle spectroscopy and single particle imaging can be combined on the same particle before and after deformation local shape and size effects can be connected to specific local plasmonic properties instead of to properties that are averaged over all particles. Examples of such properties are the flattening of the Au nanorods on only one side and a reduction in particle volume for some particles. Electron energy-loss spectroscopy (EELS) has recently proven to be a good technique for imaging local plasmonic properties of metallic nanoparticles. It has become possible to perform a local mapping of the plasmon resonances of single metal nanoparticles of various different shapes at a high resolution in energy and space^{36–42}, additionally coupling of resonances of particles that are near each other has been analyzed as well^{36,37}.

It is well known that coatings surrounding gold nanorods can greatly influence the deformation behavior. Such coatings are often used to increase the colloidal stability of Au nanoparticles in solution as these metals are characterized by large Hamaker constants and thus large van der Waals attractions inducing aggregation. So far, mainly heat-induced particle deformation experiments were conducted to understand the influence of coatings on the deformation of gold nanorods^{43,44}. It was shown for instance that a thin carbon layer can drastically increase the thermal stability of a Au nanorod⁴⁵. Silica is an important coating since it can enhance the thermal, mechanical and colloidal stability. Furthermore, it can be made mesoporous and thus the particle’s surface is still available for catalytic reactions and/or for sensing applications^{8,46–48} and additionally drugs can be efficiently transported

due to a large surface area in the mesoporous shell²¹.

Surprisingly, however, little effort has been made to study the heat-induced deformation behaviour of silica coated gold nanorods. Recently, it was shown that the thermal stability for oven heated rods can be drastically enhanced by a mesoporous silica-coating⁴⁹. Under illumination of ns-pulses mesoporous silica-coated gold nanorods were shown to be more stable as well^{50,51}. Also, for photoacoustic imaging silica-coated gold nanorods are promising candidates since coating the Au nanorods with silica improved the imaging properties^{52,53}. Finally, for cancer treatment therapies silica-coating of gold nanorods enhanced the performance. Zhang et al. showed that chemotherapeutic drug release was significantly improved and that hyperthermia is also possible for coated nanorods²¹.

Looking at the many possible application improvements of silica-coated gold nanorods, fundamental research on how such layers influence the deformation properties is needed. Single-particle measurements can help to unravel on a microscopic level the deformation process and the influence of a silica shell. As far as we know, these are the first single-particle deformation experiments of silica-coated gold nanorods under illumination of fs-laser pulses. The experiments were analysed by transmission electron microscopy (TEM) and EELS. Our method allows for specifically deforming single particles in 3D assemblies⁵⁴ which can lead to new applications like the modification of metallo-dielectric photonic crystals.

Results and discussion

It is well known that the position of the plasmon peak depends on the surrounding medium^{1,25,55}. Thus, in order to optimally excite the gold nanorods at their longitudinal plasmon resonance in our confocal setup the refractive index change from ethanol to glycerol needs to be taken into account. In glycerol the longitudinal plasmon peak is red-shifted by about 30 nm to 860 nm (Figure S1) with respect to ethanol. For the deformation experiments the excitation was therefore fixed at 860 nm but the power was varied. The laser power is directly con-

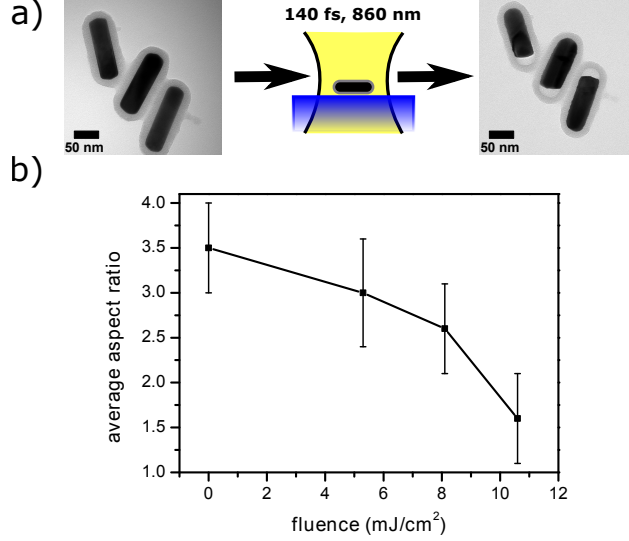


Figure 1: a) illustrates the schematic experimental setup and shows typical TEM images of Au NRs before and after deformation. b) shows the average aspect ratio after an applied laser power. The change in aspect ratio was averaged over about 100 particles. The initial average aspect ratio of the rods were 3.4 ± 0.5 coated with a 14 nm thick silica shell.

nected to the temperature the particle is heated to^{29,32,56} and thus the degree of deformation strongly depends on the applied laser power.

For different laser powers the aspect ratio and shape of the same particles before and after laser irradiation were determined by TEM. By averaging over several particles for each applied laser power a general dependence on the degree of deformation was determined. Such an average is helpful to compare our measurements with previous studies. A typical outcome for different laser powers is shown in Figure 1b where the average aspect ratio of three different areas on the same TEM grid of silica coated gold nanorods illuminated at three different values of the laser power was averaged over about 100 particles. At the lowest fluence of 5.3 mJ/cm^2 the average aspect ratio decreased to about 3.0. With increasing fluence the average aspect ratio was further reduced to about 2.6 for 8.1 mJ/cm^2 and to 1.6 for 10.6 mJ/cm^2 . The laser power that we used is generally much lower than Chen et al. reported when using ns-laser pulses to deform silica-coated gold nanorods where changes in the absorption spectrum only occurred at 20 mJ/cm^2 for $34 \text{ nm} \times 9 \text{ nm}$ sized rods with a 20 nm thick silica shell⁵⁰. This relates to the fact that fs-heating is more efficient than ns-heating as

the total energy from the laser pulse can be transferred to the crystal before lattice cooling takes place. For uncoated gold nanorods Link et al. also reported that fs-heating requires less laser power compared to ns-heating^{28,29}. In our experiment many more laser pulses were supplied than needed for deformation as gold nanorods with an average size of $92\text{ nm} \times 30\text{ nm}$ but without a rigid shell could be even deformed by single fs-laser pulses with the degree of deformation being dependent on the fluence³⁴. As we see a dependence on the provided fluence the deformation process must be self-limiting in the sense that the laser light is not efficiently absorbed anymore once the aspect ratio drops below a certain value shifting the plasmon resonance out of the wavelength range of the laser excitation pulse. For example, at 5.3 mJ/cm^2 the average aspect ratio dropped to 3.0 leading to a longitudinal plasmon shift of about 25 nm (details Figure S1) which will thus be shifted out of the excitation pulse.

The curve in Figure 1b follows a similar trend as measurements from Zijlstra et al³⁴. They performed single particle deformation experiments on gold nanorods without silica coating but embedded in a PVA film. For particles with an aspect ratio of 3 ($92\text{ nm} \times 30\text{ nm}$) they found partial melting to start around 1.3 mJ/cm^2 and complete melting at 1.85 mJ/cm^2 . From that they calculated a melting energy of $Q_{melt} = 260\text{ fJ}$ which is 15% higher than following thermodynamic considerations where they calculated Q_{melt} to be 225 fJ according to

$$Q_{melt} = \rho V [c_p (T_{melt} - T_0) + \Delta H_{fus}] \quad (1)$$

where ρ is the density of gold, V the Au volume of the nanorod, c_p the specific heat capacity of gold, T_{melt} the melting temperature of gold, T_0 the ambient temperature and ΔH_{fus} the heat of fusion for gold. The authors attributed the higher stability in experiments to the viscoelasticity of the PVA polymer matrix surrounding the particles, which hinders surface-driven migration, and to heat dissipation.

The energy Q_{abs} that is absorbed by a particle with an absorption cross section σ_{abs} under

a laser fluence F is calculated by using

$$Q_{abs} = \sigma_{abs} F. \quad (2)$$

The absorption cross section for a gold rod is available as an analytical expression from Mie-Gans theory for a spheroidal shape³²:

$$\sigma_{abs} = \frac{2\pi V}{3\lambda} \epsilon_m^{3/2} \sum_j \frac{\left(1/P_j^2\right) \epsilon_2}{(\epsilon_1 + (1 - P_j) \epsilon_m/P_j)^2 + \epsilon_2^2} \quad (3)$$

where ϵ_1 and ϵ_2 are the real and imaginary part of the dielectric constant of gold, respectively, and ϵ_m is the dielectric constant of the medium. The depolarization factors P_j are given by

$$P_A = \left(\frac{1 - e^2}{e^2} \right) \left\{ \frac{1}{2e} \ln \left(\frac{1 + e}{1 - e} \right) - 1 \right\} \quad (4)$$

$$P_B = P_C = \frac{1 - P_A}{2} \quad (5)$$

where $e = \sqrt{1 - 1/(L/W)^2}$ is the eccentricity and L/W is the aspect ratio of the rod.

However, calculating a reliable absorption cross section is difficult since the analytical Mie-Gans theory, which is only available for particles with an ellipsoidal shape, does not accurately model experimental nanorods as not only the aspect ratio alone influences the extinction spectra but also end-cap geometries and the volume of the rods⁵⁷. Prescott et al. showed that by adjusting the depolarization factors, reasonable results for the plasmon excitation wavelengths can be obtained (Figure S1). However, for obtaining absorption intensities experimental data are so far quantitatively more reliable. Zijlstra et al. measured experimental scattering cross sections for single gold nanorods with an average size of $5.8 \cdot 10^4 \text{ nm}^3$ and calculated the according absorption cross section by multiplying by the intensity ratio³⁴. Using their values and using a correction factor of 1.7 to account for the volume difference we can estimate Q_{abs} by $Q_{abs} = F \cdot 11.3 \cdot 10^{-11} \text{ cm}^{-2}$. However, this rep-

resents the absorbed energy when the particle is oriented along the polarization of the laser beam. If the particle is oriented perpendicular it will absorb almost no energy. Our particles are randomly distributed with respect to the polarization and will thus only absorb about 1/2 of that energy. For the experimentally applied fluences of 5.3 mJ/cm², 8.1 mJ/cm² and 10.6 mJ/cm² the particles thus absorb approximately 300 fJ, 460 fJ and 600 fJ on average. The required melting energy calculated by equation 1 is 380 fJ for our rods. Thus, for the highest applied laser fluence (where particles are still not all completely deformed to a spherical shape) the particles absorb about 55% more energy than required for melting which is a lot more than the 15% that Zijlstra et al measured for uncoated rods in PVA.

The increased stability is probably due to two reasons. First, heat diffusion is faster for silica-coated gold nanoparticles compared to particles without a silica shell. Hu et al. measured a decrease in the characteristic heat dissipation time constant after coating spherical gold nanoparticles with a thin silica shell in water compared to uncoated particles in water²⁶. The characteristic heat dissipation time depends on the size of the particle and the thermal properties of the surroundings (details in SI). Hu et al. measured a time constant of 55 ps for a spherical gold particle with a thin silica shell in water. Taking different sizes and thermal properties of the solvent into account we roughly estimate a characteristic heat dissipation time of about 500 ps for our system (SI). The same estimation leads to a time constant of about 2000 ps for the particles in³⁴. Thus, heat gets dissipated faster away for our system. However, it was shown that structural transformations occur on fast time scales as well. Plech et al. inferred from their measurements that complete melting of 100 nm sized spherical particles in water (which is comparable in volume to our rods) occurred within 100 ps (their time resolution limit)⁵⁸. Link et al. concluded from pump-probe absorption measurements that melting of micelle-capped gold nanorods in solution takes 30-35 ps⁵⁹. Their nanorods were about 25 to 50 times smaller than ours. Thus, from literature it can be estimated that structural transformations for sizes of our rods can happen between 35 ps and 100 ps. Thus, heat dissipation is probably not the main reason for the increased stability.

Another influence of the silica shell is its rigidity which hinders the migration of surface atoms and in addition hinders a shape change which does not fit in the original shell diameter. External oven heating measurements performed by Gergely-Fülöp and coworkers confirmed that⁴⁹ as well as measurements performed in our group⁶⁰. In their work heat diffusion does not play a role due to the long time scales involved. For an aspect ratio of 3.4 (30 nm \times 9 nm, 15 nm mesoporous silica shell) particles deformed to an almost spherical shape after heating at 700°C for one hour. In comparison, uncoated nanorods with an aspect ratio of 3.3 (73 nm \times 22 nm) already completely deformed to spherical particles after heating at 250°C for one hour³². Thus, the silica-coated nanorods were stable to almost three times higher temperatures despite the significantly smaller volume and thus smaller surface to volume ratio. Therefore, it is likely that the enhanced stability for our rods is mostly influenced by the hindrance of surface atom movement and the confinement effects of the silica shell that has to deform to accommodate thicker rods.

The different absorbed energies are not only reflected in the changed aspect ratio but also in the shape of the resulting particles both with respect to the geometry of the gold core and silica shell. Figure 2 shows the same particles before (upper row) and after (bottom row) deformation where particles in different columns absorbed different energies (increasing from left to right). The corresponding aspect ratio changes are summarized in table 1.

The amount of energy each single particle absorbs can vary strongly since it depends on the exact position of the particle with respect to the laser beam. Since the laser beam is scanned over the sample some particles will end up right in the middle of the beam and thus absorb more energy as particles that are away from the middle. The z-position of the particle also plays an important role here. The substrates are not perfectly flat and different particles will experience small differences in z-position. Since the laser beam goes through an objective with a high numerical aperture different z-positions experience different powers. The intensity variation is expressed in the point spread function of the microscope used and has recently been measured for this system⁶¹. For example, for 17 pJ pulse energy the fluence

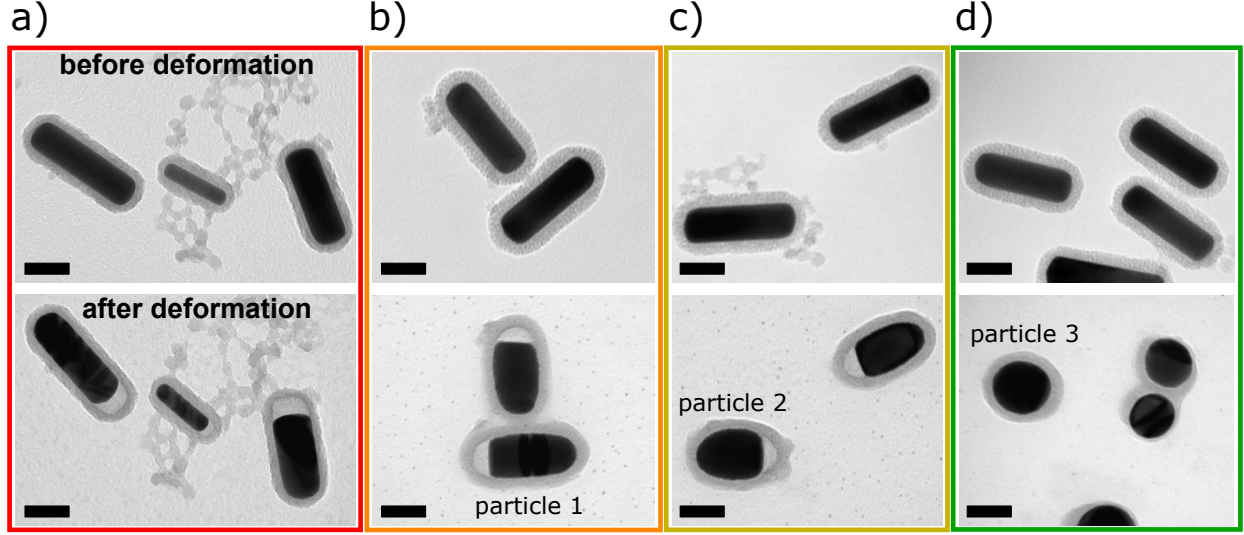


Figure 2: Comparison of the same particles before (upper row) and after (bottom row) deformation for average fluences of a) 5.3 mJ/cm^2 and b)-d) 10.6 mJ/cm^2 (with differently absorbed energies, see text for clarification). The different columns show different stages of deformation. The absorbed energy increases hereby from left to right. The aspect ratios before and after deformation are summarized in table 1. EELS measurements presented in Figure 3 were performed on the exact same particles marked with the name particle 1 to 3. All scale bars are 50 nm.

is 5.3 mJ/cm^2 in the focal plane and drops to 4.0 mJ/cm^2 for a z-position 240 nm below or above the focal plane (details in SI) changing z might not have a significant influence since the particles already absorbed energy and consequently their longitudinal plasmon resonance shifted out of the excitation wavelength of the laser. Although the sample was scanned in a small 3D stack (starting from the 2D focal plane determined in reflection mode) Another important factor that influences the amount of absorbed energy is the orientation of the NR with respect to the laser polarization. Particles that are aligned with the polarization will absorb more energy than particles that are not aligned³⁵. Additionally, the polydispersity of the sample will influence the absorption behaviour. If the longitudinal peak position of one particle does not optimally match the excitation wavelength it will absorb less energy. The above mentioned points are reflected in the relatively large error bars, obtained from the standard deviation, observed in Figure 1. Hence, calculating a temperature that can be ascribed to a single particle is difficult and will be inaccurate, also because heat accumulation

Table 1: Aspect ratios before and after deformation for the particles from Figure 2 going from left to right.

	a)	b)	c)	d)
before deformation	3.6	3.0	3.2	2.9
	4.3	3.0	3.5	2.9
	3.0			3.2
after deformation	3.0	1.6	1.3	1.0
	3.6	2.0	1.6	1.0
	2.2			1.0

in the dispersion medium can play a role for high-repetition laser systems. Zijlstra et al. showed that the threshold to deform and damage particles increases with higher numerical aperture objectives⁵². This was explained by the larger surface to volume ratio resulting in better heat dissipation for smaller focal spots. In our setup heat accumulation might not play a major role since we have a highest numerical aperture and thus a large surface to volume ratio of the focal spot. Furthermore, since the focal spot is small only single particles or at most three particles will be in the focal spot which has a diameter of 320 nm in the focal plane for our settings and thus merging of the single heat baths was a minor issue.

Due to the considerations above, it cannot be determined which precise energy each single particle in Figure 2 absorbed but the amount of absorbed energy clearly increases from the left column to the right column since the deformation is enhanced. It can be seen that the particles deform from a rod-shape via an intermediate bullet-shape to a final spherical shape. Particles in column (a) only deformed slightly and adopt a rod shape which is shorter and wider than the original particles. Since the shell is mesoporous it can most likely densify without changing its overall shape too much. But also, if forced, shape changes are more easily possible compared to a solid shell without internal pores. This is supported by the observation that the mesoporosity is reduced after deformation. The shape in the first column is mainly observed for the lowest used laser fluence of 5.3 mJ/cm².

Particles in columns (b)-(d) were irradiated with an average fluence of 10.6 mJ/cm² but different absorbed energies following the discussion above. The larger deformations could

only be achieved by deforming the silica as well to make enough room for the larger width of the gold particle. Thus, the significantly reduced porosity of the shell did not give enough space for the gold particle to deform. The observed intermediate gold shapes as in column (b) and (c) were bullet-shaped. There is still room between the gold rod and the silica shell at the flat end of the particle. It is remarkable that in no case we observed a change in rod shape on both ends of the Au particles which remained flush with the silica shell on one end. An intermediate shape has not been so clearly and abundantly observed so far and as mentioned it is interesting that only one end was found to flatten and detach from the silica shell. Some groups reported intermediate ϕ -shapes although this was mainly observed for ns-pulses and particles without a solid shell^{27,29}. Chon et al. reported an intermediate dumbbell-like structure⁶² after fs-laser pulse illumination for initial rods with an aspect ratio of 4, a silica-shell thickness of 35 nm and a smaller volume than our rods (no exact volume was provided but from the TEM image it can be estimated to be 15 times smaller than our volume). They argued that the structure occurred since the melting started at both tips of the rods and stopped before a transformation to a spherical shape was completed. The exact intermediate shape most likely depends on the surface-to-volume ratio, shell thickness or initial aspect ratio of the rod as well. Research to get more insight in what is important for what shape change is ongoing and the focus of a next paper. In case of complete deformation to a spherical gold particle (column d)) the silica is also completely deformed and was found to remarkably still enclose the spherical gold particles.

The changes in aspect ratio were accompanied by a change of the longitudinal plasmon resonance which we measured by EELS. First, we measured particles before laser irradiation which is shown in Figure 3a. The upper left image in Figure 3a is the dark field image of the particles including two colored markers for the spots where the spectra were extracted that are shown in the upper right Figure of 3a. The spectrum recorded at the blue position shows a strong resonance at 1.55 eV (800 nm) which is the longitudinal plasmon resonance. The spectrum which was recorded at the red spot shows a peak at 2.4 eV (520 nm) which

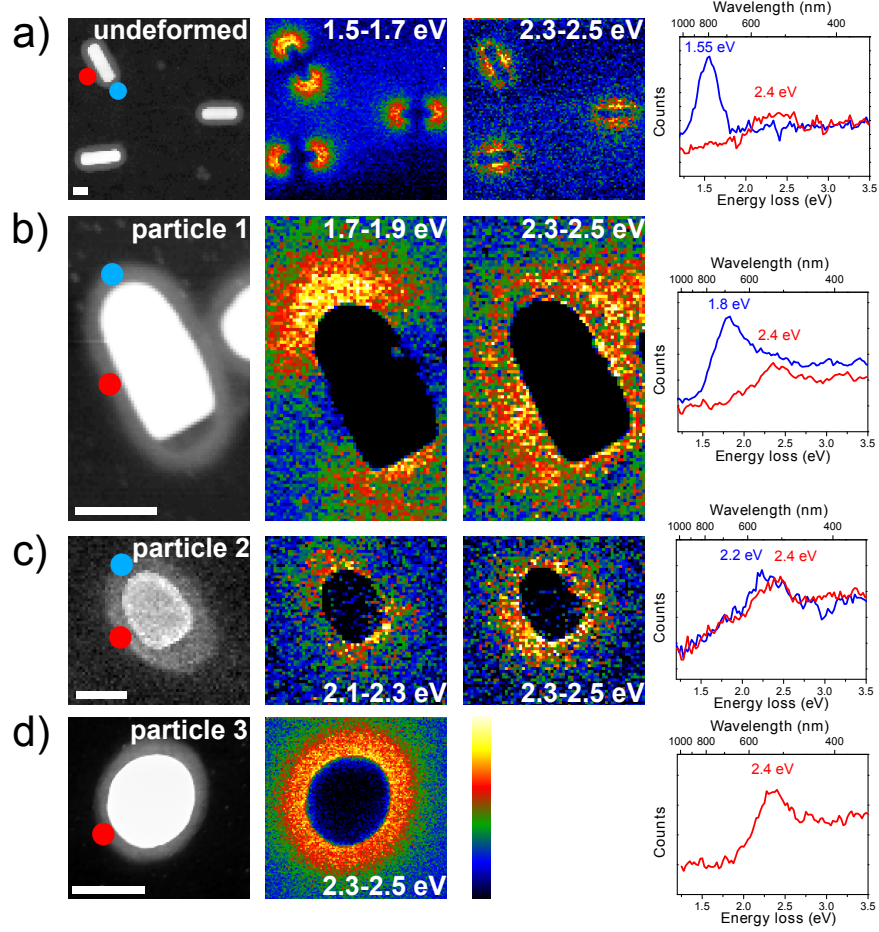


Figure 3: EELS measurements of undeformed (a), partially deformed (b),(c) and completely deformed nanorods (d). The same particles which are shown in Figure 2 are presented here. The longitudinal plasmon resonance is blue-shifted with higher degree of deformation. The plasmon maps show the longitudinal and transverse character. All scale bars are 50 nm.

corresponds to the excitation of the transverse plasmon resonance. Comparing these measurements to the measured extinction spectrum in solution (Figure S1) one can see that the plasmon peak positions measured by EELS are blue-shifted. These shifts can be explained by the different dielectric media as the EELS measurements were performed in vacuum. When inserting a dielectric constant of vacuum, the same longitudinal peak position is obtained (Figure S1). The two resonance energies were mapped locally which resulted in the two lower images of Figure 3a. The longitudinal and transverse characters can be clearly identified and agree with previous EELS measurements of gold nanorods^{36,37,39}.

The EELS measurements of the deformed particles were taken and plotted in the same

way as described above for the undeformed ones. Figure 3b shows the measurement of the deformed particle which is marked as particle 1 in Figure 2. The longitudinal plasmon resonance was found to be blue-shifted to 1.8 eV (690 nm) which corresponds to the observed decrease in aspect ratio with respect to the undeformed particles which exhibited a resonance at 1.55 eV (800 nm). The transverse plasmon resonance stayed at 2.4 eV. The plasmon maps for both energies still show a clear longitudinal and transverse character which is preserved after deformation. It can furthermore be seen that the flatter side of the rod exhibits a less pronounced signal than the tip-shaped end of the rod. This is in agreement with the lightning rod effect and is reproduced by FDTD simulations presented in Figure S3 where the longitudinal resonance (signal at 694 nm) is depicted. As in the experiments it exhibits a stronger local field enhancement at the round tip of the rod and a less enhanced one at the flat end. Due to the sharp corners in the simulations the two corners at the flat side also show strong local field enhancements. For the experimental rod these corners were more rounded and not as sharp and thus no such strong enhancements were observed at these corners.

The EELS measurement results for particle 2 of Figure 2 are shown in Figure 3c. The longitudinal plasmon resonance was shifted to 2.25 eV (551 nm) and starts to overlap with the transverse one. The plasmon maps still exhibit a longitudinal and transverse character but the spatial extent of both resonances cannot be as nicely resolved as for 4a and b due to the limited energy and spatial resolution. As observed for the particles in Figure 3b the flatter end of the rods have a less pronounced plasmonic field enhancement than the rounded tip of the rods. This difference, however, is less pronounced in Figure 3c due to the overlap of the longitudinal and transverse resonances which makes it more difficult to separate the two signals for this smaller aspect ratio. As expected, for a complete deformation into a nanosphere only one plasmon resonance at 2.4 eV (520 nm) was observed. As is quite clear from the excitation maps this resonance is spread out over the whole particle.

Our methodology allows us to not only observe changes in the particles aspect ratio and

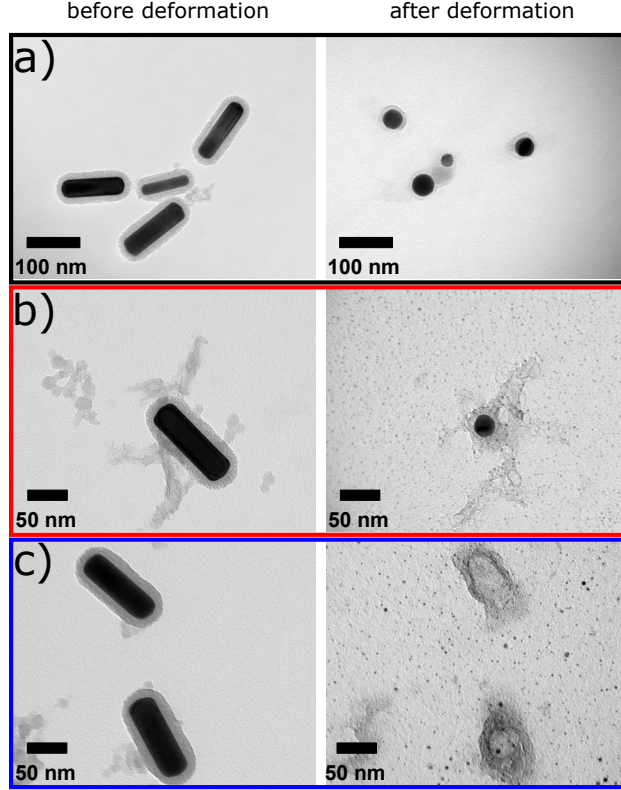


Figure 4: Au volume loss at higher fluences. a) and b) show particles that reduced in size after being illuminated with a fluence of 10.6 mJ/cm^2 . For a fluence of 13.8 mJ/cm^2 most particles disappear (c). b) and c) furthermore show examples of cluster formation which increases with increasing fluence.

shape but also to make estimates of the volumes before and after deformation. We estimated the volume from the 2D shape and sizes that we measure from the TEM images. It needs to be mentioned that an exact volume determination is only possible in 3D. 3D tomography has been done on gold nanorods and makes it possible to determine the exact volume⁶³. For undeformed rods the known geometry was used to determine the volume. For deformed particles the volume could be estimated assuming that due to the 3D confinement of the silica shell the particles deforms similarly in the third dimension.

With higher laser intensities a fraction of the particles was found to lose part of their volume during the laser deformation. Up to a fluence of 8.1 mJ/cm^2 the particles did not show any volume changes. Thus, volume changes roughly started to occur for a small percentage of particles for absorbed energies above the melting threshold. We hereby allow

a $\pm 15\%$ discrepancy for the volume due to uncertainties which occur when measuring the diameter and length of the nanorod from TEM images and from small irregularities in shape of the deformed particles. At higher pulse energies many particles were found to be reduced in size. For instance, for the measurement presented in Figure 1b about one third of the particles suffered from a size reduction for a fluence of 10.6 mJ/cm^2 . Those particles were not included in the analysis since a volume loss can influence the aspect ratio change. Again it needs to be stressed that this is only a rough estimate since we calculate the volume based on a 2D projection. Examples of particles that underwent more severe size reductions are shown in Figure 4a. The same four particles before and after deformation are shown. All particles completely deformed to a spherical shape. However, all volumes dropped to less than one third of the volumes of the original rods, based on the 2D projection. At higher laser fluences more and more particles underwent a size reduction up to a point where all particles lost volume. A size reduction and laser ablation of gold nanoparticles upon laser irradiation is well known in literature^{64–66}, also for fs-pulse irradiation where they used micelle-stabilized rods with a volume 26 times smaller than ours²⁸. Those experiments were performed at higher fluences (about 200 J/cm^2), though, despite the smaller volume. Thus, the size reduction needs to be taken into account for photothermal applications as we found it to also happen for increasing percentages of particles at lower fluences despite the mesoporous silica coating. Such effects would be hard to detect without our single particle analysis where the same particles are observed before and after deformation.

Particles that were reduced in size were often accompanied by the presence of small gold droplets on the surface of the TEM grid which can be seen in Figure 2 already. This strengthens the point made by calculating the volumes of the particles from the 2D projections that the particles lose volume. It should be stressed that these small particles are most likely not present in the Au NR solution as the TEM images before deformation prove. We verified that the droplets are gold by high-resolution TEM (Figure S4). The volume of clusters found on the grid was found to increase for higher fluences, not necessarily in the number of clusters

but rather in their size. Figure 4b and c show an example of the clusters seen for fluences of 10.6 mJ/cm^2 and 13.8 mJ/cm^2 , respectively. What is also clear from Figure 4c is that at higher fluences (higher than 10.6 mJ/cm^2) many particles completely disappeared. The gold particle was completely gone and only part of the silica shell still remained. It does not necessarily mean that the particle was heated above the boiling temperature of gold (around 3100 K). Fragmentation can happen at temperatures below the melting point even⁶⁷. At high temperatures the silica shell can also break and release the gold⁴⁹. Thus, the main part of the gold fragments was probably lifted to the surrounding glycerol with a subsequent transport away from the illuminated spot by Brownian motion and/or thermophoresis, as otherwise a lot more material would have been deposited around the remaining silica shell.

In principle, the mesopores of the silica shell are big enough to allow material transport. Thus, it seems that a lot of gold penetrated the shell through the mesopores and was deposited around the particle or transported away in the surrounding liquid. To check whether that could be the case we coated a small part of the sample with a more dense Stoeber silica shell on top of the mesoporous shell closing off the pores and resulting in a total shell thickness of about 19 nm . Thus, close to the rod the shell was more mesoporous than at the outer part of the shell. We observed that small gold fragments ended up inside the shell (Figure S5), even before a significant volume reduction took place. The clusters did not necessarily penetrate through the shell as a whole but they could also be in forms of ions and later on forming clusters in the surrounding solution and finally precipitating after drying.

In conclusion, we performed single particle deformation experiments on silica-coated gold nanorods under fs-illumination analyzing both shape and plasmon resonances by electron microscopy. Silica-coated rods were found to be more stable compared to uncoated rods and deform via an intermediate bullet-like shape where one end of the rod was found to detach from the mesoporous silica shell and become flatter than the other end which remained attached to the silica shell. These morphological changes were also reflected in the plasmonic properties, which were confirmed by FDTD calculations taking the observed shape as input.

A less pronounced longitudinal resonance and thus local field enhancement was measured and calculated at the flatter side. Furthermore, size reduction of the particles was observed, also for a certain percentage of particles that were not completely deformed yet and at relatively low fluences. Our measurements pave the way towards understanding the deformation behaviour of single gold nanorods under a mesoporous silica shell constraint and are therefore of importance for all the applications where a shell enhances properties, also specifically for our future project in which we want to tailor the plasmonic resonances of single particles in 3D photonic assemblies in similar ways as a DVD disk can be written in a 2D fashion.

Methods

Gold nanorods were synthesized following the method of Ye et al.⁶⁸. The average aspect ratio and volume of the rods were 3.4 ± 0.5 and $(9.9 \pm 0.4) \cdot 10^4 \text{ nm}^3$, respectively. The rods were then coated with a 14 nm thick mesoporous silica shell following the method of Gorelikov and Matsuura⁶⁹. The coated particles were stored in ethanol. Shell thickness and particle sizes and the polydispersity were determined by analyzing TEM images of about 330 particles.

In order to achieve local single particle laser-induced heating a Leica SP8 confocal setup (63x/1.4 oil-immersion confocal Leica objective) equipped with both, a Coherent chameleon II Ti:Sapphire laser (80 MHz repetition rate, 140 fs pulse length) and a fiber-based white light laser, was used. For the laser-induced deformations, a drop of the particle dispersion was dropcasted on a TEM finder grid. TEM images of all particles in a spot of about $12 \mu\text{m} \times 12 \mu\text{m}$ were taken with a TECNAI12 electron microscope. The grid was then placed on a microscopy slide. Subsequently, glycerol was put on top of the grid to reduce the scattering of the silica (refractive index of 1.45), while also being close to the index of the immersion oil and glass (refractive index of 1.51). This sample system was then closed with a 0.1 mm thick cover glass. The white light laser at the 480 nm laser line was used in reflection mode

to find back the spot which was looked at by the TEM before and to focus onto the right z-plane. For the laser-induced heating a thin 3D stack with 2D planes of $11.5\text{ }\mu\text{m} \times 11.5\text{ }\mu\text{m}$ was scanned by the Ti:Sapphire laser at 860 nm with a pixel size of $22.6\text{ nm} \times 22.6\text{ nm}$ and a pixel dwell time of $1.2\text{ }\mu\text{s}$ (400 Hz scanning speed). The simulated axial and longitudinal point spread functions for this specific setup can be found in the supporting information. After illumination the glycerol was removed by drying the TEM grid in vacuum overnight. The particles of the same spot were imaged in the TEM afterwards. This enabled us to study the heat-induced deformation on a single particle level and to analyze the same particles before and after deformation. The method is illustrated in Figure 1a. The time-averaged laser power was measured by a Thorlabs PM200 powermeter using a Thorlabs S170C microscope slide power sensor.

EELS measurements were performed on a monochromated aberration-corrected microscope operated at 120 kV. Using a monochromator, an energy resolution of 150 meV was obtained as measured by the width at half maximum of the zero loss peak. For the acquisition of the plasmon maps, a pixel size of 1.3 nm is used with a spectrum collection time of 0.03 s. In order to analyze the recorded EELS data cubes, a power law background subtraction was performed using Digital Micrograph 2.3.0. Plasmon maps are then obtained using an energy selecting window that is positioned at the desired energy losses corresponding to the different plasmon modes. The FDTD simulations were performed with the software FDTD solutions 8.12.590 from Lumerical Solutions. We used the dimensions as measured by TEM after deformation for particle 1 in Figure 2b and a mesh size of 0.5 nm.

Acknowledgement

We thank Dr. Nicolas Gauquelin for his assistance during the EELS measurements and Thomas Atlantzis for the high-resolution images of the gold clusters. The authors acknowledge financial support from the European Research Council under the European Unions

Seventh Framework Programme (FP-2007-2013)/ERC Advanced Grant Agreement #291667 HierarSACol and the Foundation of Fundamental Research on Matter (FOM), which is part of the Netherlands Organisation for Scientific Research (NWO). The authors furthermore acknowledge financial support from European Research Council (ERC Starting Grant #335078-COLOURATOMS). The authors also appreciate financial support from the European Union under the Seventh Framework Program (Integrated Infrastructure Initiative N. 262348 European Soft Matter Infrastructure, ESMI). This work was supported by the Flemish Fund for Scientific Research (FWO Vlaanderen) through a postdoctoral research grant to B.G.

Supporting Information Available

Measured and calculated extinction spectra, estimate of heat dissipation time, confocal point spread functions, FDTD simulations, more details on size reduction and cluster analysis.

This material is available free of charge via the Internet at <http://pubs.acs.org/>.

References

- (1) Pérez-Juste, J.; Pastoriza-Santos, I.; Liz-Marzán, L. M.; Mulvaney, P. *Coord. Chem. Rev.* **2005**, *249*, 1870–1901.
- (2) Huang, X.; Neretina, S.; El-Sayed, M. A. *Adv. Mater.* **2009**, *21*, 4880–4910.
- (3) Zijlstra, P.; Orrit, M. *Reports Prog. Phys.* **2011**, *74*, 106401.
- (4) Vigderman, L.; Khanal, B. P.; Zubarev, E. R. *Adv. Mater.* **2012**, *24*, 4811–4841.
- (5) Li, N.; Zhao, P.; Astruc, D. *Angew. Chemie - Int. Ed.* **2014**, *53*, 1756–1789.
- (6) Li, P.-C.; Huang, S.-W.; Wei, C.-W.; Chiou, Y.-C.; Chen, C.-D.; Wang, C.-R. *C. Opt. Lett.* **2005**, *30*, 3341–3343.

- (7) Li, P.-C.; Wang, C.-R. C.; Shieh, D.-B.; Wei, C.-W.; Liao, C.-K.; Poe, C.; Jhan, S.; Ding, A.-A.; Wu, Y.-N. *Opt. Express* **2008**, *16*, 18605–18615.
- (8) Son, M.; Lee, J.; Jang, D. J. *J. Mol. Catal. A Chem.* **2014**, *385*, 38–45.
- (9) Takahashi, H.; Niidome, Y.; Yamada, S. *Chem. Commun.* **2005**, 2247–2249.
- (10) Sudeep, P. K.; Joseph, S. T. S.; Thomas, K. G. *J. Am. Chem. Soc.* **2005**, *127*, 6516–6517.
- (11) Li, C.-Z.; Male, K. B.; Hrapovic, S.; Luong, J. H. T. *Chem. Commun.* **2005**, 3924–3926.
- (12) Alvarez-Puebla, R. A.; Agarwal, A.; Manna, P.; Khanal, B. P.; Aldeanueva-Potel, P.; Carbó-Argibay, E.; Pazos-Pérez, N.; Vigderman, L.; Zubarev, E. R.; Kotov, N. A.; Liz-Marzán, L. M. *PNAS* **2011**, *108*, 8157–8161.
- (13) Sivapalan, S. T.; Devetter, B. M.; Yang, T. K.; Dijk, T. V.; Schulmerich, M. V.; Carney, P. S.; Bhargava, R.; Murphy, C. J. *ACS Nano* **2013**, *7*, 2099–2105.
- (14) Mansuripur, M.; Zakharian, A. R.; Lesuffleur, A.; Oh, S.-H. H.; Jones, R. J.; Lindquist, N. C.; Im, H.; Kobayakov, A.; Moloney, J. V. *Opt. Express* **2009**, *17*, 14001–14.
- (15) Taylor, A. B.; Kim, J.; Chon, J. W. M. *Opt. Express* **2012**, *20*, 5069–5081.
- (16) Ullah, A.; Li, X.; Cheng, X.; Hao, X.; Su, Y.; Ma, J.; Gu, M. *Opt. Express* **2012**, *20*, 2362–2368.
- (17) Zijlstra, P.; Chon, J. W. M.; Gu, M. *Nature* **2009**, *459*, 410–413.
- (18) Kennedy, L. C.; Bickford, L. R.; Lewinski, N. A.; Coughlin, A. J.; Hu, Y.; Day, E. S.; West, J. L.; Drezek, R. A. *Small* **2011**, *7*, 169–183.
- (19) Akiyama, Y.; Mori, T.; Katayama, Y.; Niidome, T. *Nanoscale Res. Lett.* **2012**, *7*, 565.

- (20) Huang, X. H.; El-Sayed, I. H.; Qian, W.; El-Sayed, M. A. *J. Am. Chem. Soc.* **2006**, *128*, 2115–2120.
- (21) Zhang, Z.; Wang, L.; Wang, J.; Jiang, X.; Li, X.; Hu, Z.; Ji, Y.; Wu, X.; Chen, C. *Adv. Mater.* **2012**, *24*, 1418–1423.
- (22) Murphy, C. J.; Sau, T. K.; Gole, A. M.; Orendorff, C. J.; Gao, J.; Gou, L.; Hunyadi, S. E.; Li, T. *J. Phys. Chem. B* **2005**, *109*, 13857–13870.
- (23) Ni, W.; Kou, X.; Yang, Z.; Wang, J. *ACS Nano* **2008**, *2*, 677–686.
- (24) Juvé, V.; Cardinal, M. F.; Lombardi, A.; Crut, A.; Maioli, P.; Pérez-Juste, J.; Liz-Marzán, L. M.; Del Fatti, N.; Vallée, F. *Nano Lett.* **2013**, *13*, 2234–2240.
- (25) Link, S.; El-Sayed, M. A. *J Phys Chem B* **1999**, *103*, 8410–8426.
- (26) Hu, M.; Wang, X.; Hartland, G. V.; Salgueiriño Maceira, V.; Liz-Marzán, L. M. *Chem. Phys. Lett.* **2003**, *372*, 767–772.
- (27) Chang, S.-S.; Shih, C.-W.; Chen, C.-D.; Lai, W.-C.; Wang, C. R. C. *Langmuir* **1999**, *15*, 701–709.
- (28) Link, S.; Burda, C.; Mohamed, M. B.; Nikoobakht, B.; El-Sayed, M. A. *J. Phys. Chem. A* **1999**, *103*, 1165–1170.
- (29) Link, S.; Burda, C.; Nikoobakht, B.; El-Sayed, M. A. *J. Phys. Chem. B* **2000**, *104*, 6152–6163.
- (30) Mohamed, M. B.; Ismail, K. Z.; Link, S.; El-Sayed, M. A. *J. Phys. Chem. B* **1998**, *102*, 9370–9374.
- (31) Al-Sherbini, A. S. A. M. *Colloids Surfaces A Physicochem. Eng. Asp.* **2004**, *246*, 61–69.
- (32) Petrova, H.; Perez Juste, J.; Pastoriza-Santos, I.; Hartland, G. V.; Liz-Marzán, L. M.; Mulvaney, P. *Phys. Chem. Chem. Phys.* **2006**, *8*, 814–821.

- (33) Link, S.; El-Sayed, M. A. *J. Chem. Phys.* **2001**, *114*, 2362–2368.
- (34) Zijlstra, P.; Chon, J. W. M.; Gu, M. *Phys. Chem. Chem. Phys.* **2009**, *11*, 5915–5921.
- (35) Taylor, A. B.; Siddiquee, A. M.; Chon, J. W. M. *ACS Nano* **2014**, *8*, 12071–12079.
- (36) Bosman, M.; Keast, V. J.; Watanabe, M.; Maarroof, A. I.; Cortie, M. B. *Nanotechnology* **2007**, *18*, 165505.
- (37) N’Gom, M.; Li, S.; Schatz, G.; Erni, R.; Agarwal, A.; Kotov, N.; Norris, T. B. *Phys. Rev. B* **2009**, *80*, 113411.
- (38) Schaffer, B.; Riegler, K.; Kothleitner, G.; Grogger, W.; Hofer, F. *Micron* **2009**, *40*, 269–273.
- (39) Schaffer, B.; Hohenester, U.; Trügler, A.; Hofer, F. *Phys. Rev. B* **2009**, *79*, 041401.
- (40) Rodriguez-Gonzalez, B.; Attouchi, F.; Cardinal, M. F.; Myroshnychenko, V.; Stephan, O.; García de Abajo, F. J.; Liz-Marzán, L. M.; Kociak, M. *Langmuir* **2012**, *28*, 9063–9070.
- (41) Myroshnychenko, V.; Nelayah, J.; Adamo, G.; Geuquet, N.; Rodríguez-Fernández, J.; Pastoriza-Santos, I.; MacDonald, K. F.; Henrard, L.; Liz-Marzán, L. M.; Zheludev, N. I.; Kociak, M.; García De Abajo, F. J. *Nano Lett.* **2012**, *12*, 4172–4180.
- (42) Nicoletti, O.; de la Peña, F.; Leary, R. K.; Holland, D. J.; Ducati, C.; Midgley, P. A. *Nature* **2013**, *502*, 80–84.
- (43) Tollan, C. M.; Marcilla, R.; Pomposo, J. A.; Rodriguez, J.; Aizpurua, J.; Molina, J.; Mecerreyes, D. *ACS Appl. Mater. Interfaces* **2009**, *1*, 348–352.
- (44) Liu, Y.; Mills, E. N.; Composto, R. J. *J. Mater. Chem.* **2009**, *19*, 2704–2709.
- (45) Khalavka, Y.; Ohm, C.; Sun, L.; Banhart, F.; Sonnichsen, C. *J. Phys. Chem. C* **2007**, *111*, 12886–12889.

- (46) Li, J. F.; Huang, Y. F.; Ding, Y.; Yang, Z. L.; Li, S. B.; Zhou, X. S.; Fan, F. R.; Zhang, W.; Zhou, Z. Y.; Wu, D. Y.; Ren, B.; Wang, Z. L.; Tian, Z. Q. *Nature* **2010**, *464*, 392–395.
- (47) Sekhar, A. C. S.; Meera, C. J.; Ziyad, K. V.; Gopinath, C. S.; Vinod, C. P. *Catal. Sci. Technol.* **2013**, *3*, 1190–1193.
- (48) Chen, J.; Zhang, R.; Han, L.; Tu, B.; Zhao, D. *Nano Res.* **2013**, *6*, 871–879.
- (49) Gergely-Fülöp, E.; Zámbo, D.; Deák, A. *Mater. Chem. Phys.* **2014**, *148*, 909–913.
- (50) Chen, Y.-S.; Frey, W.; Kim, S.; Homan, K.; Kruizinga, P.; Sokolov, K.; Emelianov, S. *Opt. Express* **2010**, *18*, 8867–8878.
- (51) Chen, L.-C.; Wei, C.-W.; Souris, J. S.; Cheng, S.-H.; Chen, C.-T.; Yang, C.-S.; Li, P.-C.; Lo, L.-W. *J. Biomed. Opt.* **2015**, *15*, 016010.
- (52) Zijlstra, P.; Chon, J. W. M.; Gu, M. *Opt. Express* **2007**, *15*, 12151–12160.
- (53) Chen, Y. S.; Frey, W.; Kim, S.; Kruizinga, P.; Homan, K.; Emelianov, S. *Nano Lett.* **2011**, *11*, 348–354.
- (54) Besseling, T. H.; Hermes, M.; Kuijk, A.; de Nijs, B.; Deng, T. S.; Dijkstra, M.; Imhof, A.; van Blaaderen, A. *J. Phys. Condens. Matter* **2015**, *27*, 194109.
- (55) Myroshnychenko, V.; Rodríguez-Fernández, J.; Pastoriza-Santos, I.; Funston, A. M.; Novo, C.; Mulvaney, P.; Liz-Marzán, L. M.; García de Abajo, F. J. *Chem. Soc. Rev.* **2008**, *37*, 1792–1805.
- (56) Baffou, G.; Quidant, R. *Laser Photonics Rev.* **2013**, *7*, 171–187.
- (57) Prescott, S. W.; Mulvaney, P. *J. Appl. Phys.* **2006**, *99*, 123504.
- (58) Plech, A.; Kotaidis, V.; Grésillon, S.; Dahmen, C.; Von Plessen, G. *Phys. Rev. B* **2004**, *70*, 195423.

- (59) Link, S.; Burda, C.; Nikoobakht, B. *Chem. Phys. Lett.* **1999**, *315*, 12–18.
- (60) van Kats, C. M. Anisotropic Model Colloids. Ph.D. thesis, Utrecht University, 2008.
- (61) Besseling, T. H.; Jose, J.; van Blaaderen, A. *J. Microsc.* **2015**, *257*, 142–150.
- (62) Chon, J. W. M.; Bullen, C.; Zijlstra, P.; Gu, M. *Adv. Funct. Mater.* **2007**, *17*, 875–880.
- (63) Goris, B.; Bals, S.; Van den Broek, W.; Carbó-Argibay, E.; Gómez-Graña, S.; Liz-Marzán, L. M.; Van Tendeloo, G. *Nat. Mater.* **2012**, *11*, 930–935.
- (64) Mafuné, F.; Kohno, J. Y.; Takeda, Y.; Kondow, T. *J. Phys. Chem. B* **2001**, *105*, 9050–9056.
- (65) Inasawa, S.; Sugiyama, M.; Koda, S. *Jpn. J. Appl. Phys.* **2003**, *42*, 6705–6712.
- (66) Muto, H.; Miyajima, K.; Mafuné, F. *J. Phys. Chem. C* **2008**, *112*, 5810–5815.
- (67) Plech, A.; Kotaidis, V.; Lorenc, M.; Boneberg, J. *Nat. Phys.* **2006**, *2*, 44–47.
- (68) Ye, X.; Zheng, C.; Chen, J.; Gao, Y.; Murray, C. B. *Nano Lett.* **2013**, *13*, 765–771.
- (69) Gorelikov, I.; Matsuura, N. *Nano Lett.* **2008**, *8*, 369–73.

Graphical TOC Entry

